Journal of Materials Chemistry C

ROYAL SOCIETY OF CHEMISTRY

PAPER

Published on 13 July 2026
Licensed under CC-BY 4.0

Check for updates

Cite this: DOI: 10.1039/d6tc01212d

Triboelectric membrane derived from adhesive chewing gum for sustainable energy and electroplating applications

Karthick Natarajan,[a] Zong-Hong Lin,[c] Priyanka Ganguly[d] and Arunkumar Chandrasekhar *[b]

Received 16th April 2026,
Accepted 10th July 2026

DOI: 10.1039/d6tc01212d

rsc.li/materials-c

Chewing gum has been a ubiquitous habit in human civilization for millennia, offering stress relief and freshness. Its widespread popularity has made it one of the most popular confectionery products globally. However, most synthetic products are water-insoluble and non-biodegradable, resulting in a staggering 250 000 tons of annual waste that also contaminates oceans, land, and ecosystems. With forecasts predicting a rise to 1 million metric tons over the next five years, the need for sustainable solutions is pressing. In response to this issue, we introduce an innovative method involving the use of recycled chewing gum in a triboelectric nanogenerator (RCG-TENG). This device can capture mechanical energy and produce an open-circuit voltage of 167 V for a device measuring 3 × 3 cm^2, a short-circuit current of 6.9 μA, and a peak power density of 35.55 μW cm^{-2}. The RCG-TENG shows potential for eco-friendly energy harvesting and industrial applications when integrated into a self-powered electroplating system. With the RCG-TENG, we achieved high-quality copper plating on top of aluminum within a short period of time using chewing gum as a triboelectric material. This research addresses microplastic pollution by converting chewing gum waste, promotes sustainable energy innovations, and aids in meeting SDG objectives, thereby promoting a more sustainable and circular economy.

Introduction

The practice of chewing gum dates back to ancient times, and chewing gum remains a widely popular confection among people of all ages and cultures worldwide. Chewing gum offers a relaxing, sensational experience that people enjoy for extended periods of time. Chewing gum is known for its ability to reduce stress and maintain the mouth with long-lasting freshness with every chew.[1] In general, chewing gum is made up of two phases: a water-insoluble part (gum base) and a water-soluble part. Chewing gum consists of either sugar or sugar-free variants.[2,3] The primary components of chewing gum include gum base, which constitutes 20–30% of the product, and synthetic elastomers, comprising 10–30%.[4] The gum base itself may be derived from natural or synthetic polymers, with polyvinyl acetate (PVAc) being a significant constituent, ranging from 15 to 45%. Synthetic elastomers, which consist of copolymers of polyisobutylene (PIB), butadiene–styrene, isobutylene–isoprene, polyethylene, and polyisoprene, play an essential role in chewing gum preparation.[3] This inactive component of the formulation supports the hydrolyzable components, which consist of (i) sweeteners, such as sucrose (which may account for up to 60% of conventional chewing gum), (ii) humectants, such as glycerin, and (iii) antioxidants, which protect other components from oxidation. (iv) Colors, flavoring agents, and organic acids are used to control the taste of chewing gum. People prefer to use "active" components such as nicotine in chewing gum as an alternative to smoking.[3,4] Each confectionery company keeps the exact amounts of these active ingredients confidential as a trade secret. These secret formulas and precise amounts are part of each brand's unique taste and competitive edge.[2,3] Chewing gum offers numerous benefits, including freshening breath, cleaning teeth, providing refreshment, increasing alertness, reducing stress, and support for quitting smoking.[5] However, some disadvantages make it slightly problematic. It is water-insoluble, nondigestible, non-biodegradable, cannot be swallowed, and is the second largest littering item in the world,

[a] School of Advanced Sciences, Vellore Institute of Technology, Vellore, Tamil Nadu, 632014, India
[b] School of Electronics Engineering, Vellore Institute of Technology, Vellore, Tamil Nadu, 632014, India. E-mail: arunkumar.c@vit.ac.in
[c] Department of Biomedical Engineering, National Taiwan University, Taipei 10617, Taiwan
[d] Applied Chemistry & Pharmaceutical Technology (ADAPT), School of Human Sciences, London Metropolitan University, London N7 8DB, UK

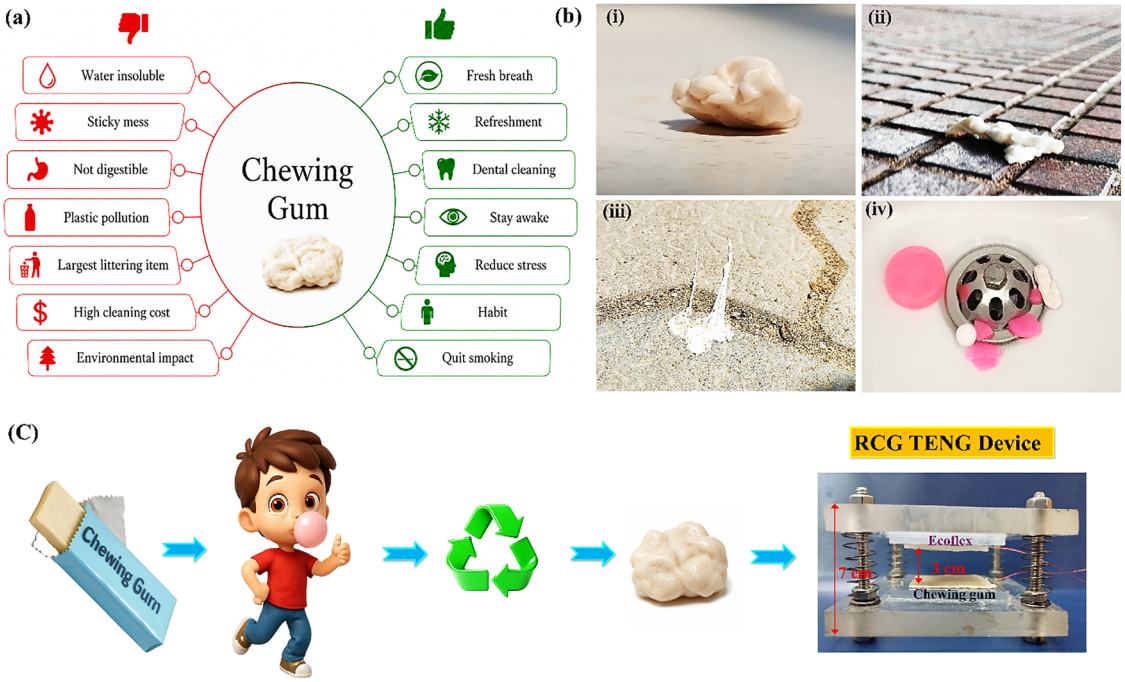

Fig. 1 (a) Detailed pros and cons of chewing gum. (b) (i–iv) Representative images depicting the pervasive pollution caused by discarded chewing gum in various urban and rural environments. (c) Schematic illustration detailing the systematic recycling of chewing gum for the fabrication of a triboelectric nanogenerator device, showcasing each stage from environmental collection to material processing to integration in sustainable energy harvesting applications.

leading to plastic pollution, a sticky mess, as well as high cleaning costs, as mentioned in Fig. 1a.[1]

According to a statistical report, Fig. S1(a) in the SI shows the global chewing gum market revenue in millions of United States dollars (US$M) for 2016 and the forecast data for 2027.[6] It shows the revenue from the chewing gum market worldwide throughout several regions, including North America, Latin America, Europe, the Middle East, and Africa. Each region's chewing gum market compound annual growth rate (CAGR) is increasing, as illustrated in Fig. S1(b), SI.[6] Revenues from the worldwide functional chewing gum market were USD 1435.7 million in 2019 and are predicted to reach USD 2831.8 million by 2027. By the year 2027, it is projected that the market will experience a CAGR of 8.9%, as depicted in Fig. S1(c) of the SI.[6] These findings indirectly indicate a continuous increase in chewing gum waste generation. Every year, chewing gum waste increases by more than 250 000 tons; however, 80–90% of the discarded chewing gum waste is not disposed of efficiently. Forecasts indicate that gum waste will reach approximately 1 million metric tons (1 metric ton = 1000 kg) in the next five years.[7] Some images of pollution threats caused by chewing gum waste on roads, public places, toilets, and pedestrian pathways of discarded sticky chewing gum are shown in Fig. 1b. It also contaminates soil, waterways, coastal regions, seas, ecosystems, and paddy crops. The authorities concerned must take responsibility for this matter to achieve a green recovery. The increasing need for sustainable energy solutions has driven innovative research into advanced technologies that can convert stored energy into usable electrical power.[8] Triboelectric nanogenerators (TENGs) are one of the most promising technologies; they can produce practical power from mechanical energy, vibrations, human movement, and wind energy.[9] Triboelectric nanogenerators operate under the theory of triboelectrification and electrostatic phenomena.[10–13] When two layers with opposite triboelectric charges tap against each other, they generate energy that can be harvested and stored in a capacitor.[14] This principle has attracted crucial attention owing to simple device structure, scalability, numerous material choices, and promise in multidisciplinary applications, including self-powered electronics, sensors, renewable energy, and other systematic real-time approaches.[15–18] Using bio-waste,[19] food waste,[20] marine bio-waste,[21] household waste,[22] medical waste,[23] textile waste,[24] and e-waste,[25] TENGs have attracted significant attention in the field of energy harvesting and the development of self-powered sensors. The existing literature explores various applications of recycled chewing gum waste. Cheng *et al.* explored its use in wearable electronics.[26] In addition, Darabi *et al.* demonstrated its potential in human body motion detection.[27] Zhao *et al.* studied its application in a self-healing electronic system,[28] and Zhu *et al.* reported its effectiveness in a self-cleaning surface for fine dust removal.[29] Nciri *et al.* examined its incorporation into road pavement material applications.[30,31] In addition, it is interesting that Gumdrop is the first company in the world to collect chewing gum waste, convert it into various useful products, and market them.[32] In different countries, a company specializing in recycling is undertaking a project to convert chewing gum into various accessories.[33]

This journal is © The Royal Society of Chemistry 2026

This study proposes a novel energetic approach for reusing chewing gum and Ecoflex film to fabricate a spring-assisted contact separation mode using a TENG. The recycled chewing gum triboelectric nanogenerator (RCG-TENG) produced a voltage of 167 V and a current of 6.9 μA. Additionally, by easily repurposing chewing gum for energy harvesting and electroplating applications, this study contributes to the Sustainable Development Goals (SDGs) by reducing microplastic environmental pollution and creating sustainable settings.

Results and discussion

X-ray diffraction analysis was used to analyse the crystallographic structure and *d*-spacing between lattice layers based on Bragg's law ($\lambda = 2d \sin\theta$). The RCG exhibited notable peaks at 23.04° (012), 29.20° (104), 31.37° (006), 36° (110), 39.45° (113), 43.12° (202), 47.58° (018), 48.47° (116), 57.43° (122), and 64.77° (300). Significant peaks in the 2θ range of 0–80° confirmed the presence of a calcium carbonate ($CaCO_3$) rhombohedral crystal structure, and the $R\bar{3}c$ space group peaks matched the crystallography of the open database COD: 1010928. The bare chewing gum (BCG) pattern showed considerable peaks at 8.1° (100), 11.51° (001), 12.58° (−101), 13.03° (110), 15.37° (011), 16.60° (200), 18.75° (111), 19.45° (210), 24.60° (−121), and 25.02° (300) in the 2θ range of 0–80°, validating the presence of sucrose ($C_{12}H_{22}O_{11}$) monoclinic crystal structure, and the *P*21 space group peaks match with JCPDS no. 00-024-1977 as shown in Fig. 2a. Fourier transform infrared (FTIR) spectroscopy effectively characterized the molecular interactions within the various components of chewing gum.[34,35] The FTIR spectrum of RCG displays multiple bands associated with its components: 3386 cm^{-1} corresponds to OH stretching (moisture), 2960 cm^{-1} and 2920 cm^{-1} relate to CH_3 asymmetric stretching (PIB, PVAc, rubber, wax), 2848 cm^{-1} indicates CH_2 symmetric stretching (PVAc, rubber, wax) and 1728 cm^{-1} is attributed to C═O stretching (PVAc).[36] The band at 1644 cm^{-1} is assigned to OH bending (moisture), 1459 cm^{-1} to CH_2 and CH_3 bending (PIB, PVAc, rubber), 1365 cm^{-1} to CH_3 bending (PIB, PVAc, rubber), 1228 cm^{-1} to C–O–C asymmetric stretching and C–$C(CH_3)_2$–C stretching (PIB, PVAc), 1015 cm^{-1} to C–O–C asymmetric stretching (PIB, PVAc),[30,31] and 605 cm^{-1} to C–CO–O bending. The FTIR spectrum of BCG verified the presence of sucrose. In the FTIR spectrum of sucrose, O–H stretching vibrations appear at 3559 cm^{-1}, 3378 cm^{-1}, and 3322 cm^{-1}. Additionally, C–H stretching vibrations were observed at 2942 cm^{-1}, whereas C–H bending vibrations were observed at 1428 cm^{-1}. The C–O–C stretching vibrations were detected at 1049 cm^{-1}, 988 cm^{-1}, and 908 cm^{-1} as depicted in Fig. 2b.[37] According to the literature, the FTIR peaks of RCG may considerably support the presence of materials such as PIB as an elastomer, PVAc as a binder, glycerin as a plasticizer, $CaCO_3$ as a filler, and sucrose as the sweetening agent.[31,35,36,38–40] Raman spectroscopy of RCG revealed significant peaks at 284, 713, and 1086 cm^{-1}, confirming the presence of calcium carbonate. Notably, the singlet peak at 1086 cm^{-1} corresponds to calcite, while the plane-bending mode of carbonate is found at 713 cm^{-1} (calcite). The Raman spectrum of BCG displayed distinct bands at 406, 548, 643, 850, 921, 1039, and 1125 cm^{-1}. These bands align closely with the Raman signatures of crystalline sucrose. For sucrose, the band at 406 cm^{-1} corresponds to aliphatic (C–C) deformation, while the 548 cm^{-1} band is associated with (C–C–O) and (C–CH_3) deformations. The band at 643 cm^{-1} is linked to alicyclic and aliphatic (C–C) vibrations. The band at 850 cm^{-1} represents (C–O–C) and alicyclic and aliphatic (CC) vibrations. The 921 cm^{-1} band involves (C–O–C) and alicyclic and aliphatic (C–C) vibrations. The 1039 cm^{-1} band is related to (C–H) ring deformation and alicyclic and aliphatic (C–C) vibrations. Finally, the band at 1125 cm^{-1} corresponds to the asymmetric (C–O–C) and alicyclic, aliphatic (C–C) vibrations, as shown in Fig. 2c.[41]

Thermogravimetric analysis, conducted in an auto-stepwise configuration, revealed a complex degradation phenomenon owing to the diverse ingredients in chewing gum. The first weight loss at 100 °C is attributed to water evaporation, whereas the second step at 150–500 °C is related to the decomposition of PVAc, PIB, and rubber. The weight loss observed between 600 and 800 °C was associated with random chain reactions, leading to lower molecular weight hydrocarbons, as shown in Fig. 2d. In mechanical studies, tensile stress tests provide insights into the stress and strain characteristics of discarded chewing gums. The sample dimensions were 1 × 3 cm^2, with a maximum stress of 0.25 MPa and a strain of approximately 40%. The same RCG sample was analyzed twice to confirm the results and ensure repeatability, as shown in Fig. 2e. The surface potential of the RCG had a positive value of 102 mV in 250 nm, as determined by Kelvin probe force microscopy (KPFM). The surface charge density (σ) was measured using $\sigma = \varepsilon_0 \times \Delta\Phi/d$, where ε_0 is the permittivity of free space (8.854×10^{-12} F m^{-1}), $\Delta\Phi$ expresses the surface potential, and d is the KPFM probe-to-surface separation gap during surface potential mapping.[42] Chewing gum has a high filler phase, sugar content (sucrose), and other components that are less polar and have a lower work function. This leads to a higher surface potential, as shown in Fig. 2f.

Surface classification based on the static contact angle measurement of a 0.6 μL water droplet on an RCG film coated on a 2 cm × 2 cm glass substrate indicates a hydrophilic property, with a measured contact angle of 61.5°, less than 90°, as shown in Fig. 2g(i). In addition, the Ecoflex film exhibited a contact angle of 105.2°, confirming its hydrophobic nature, as illustrated in Fig. 2g(ii). Silicone elastomers, such as Ecoflex, are also known for their anti-adhesive nature, as the methyl-rich silicone backbone creates a chemically inert surface with few polar interaction sites. This indicates that chewing gum cannot form strong adhesive bonds with the Ecoflex surface, making it easy to contact and separate despite the gum's inherent stickiness.[43] Fig. 2h illustrates a scanning electron microscopy (SEM) image that reveals the rubbery and elastic morphology of the chewing gum waste, observed at a magnification of 20 μm. To evaluate the biodegradation characteristics of the RCG, an eight-month soil burial test was

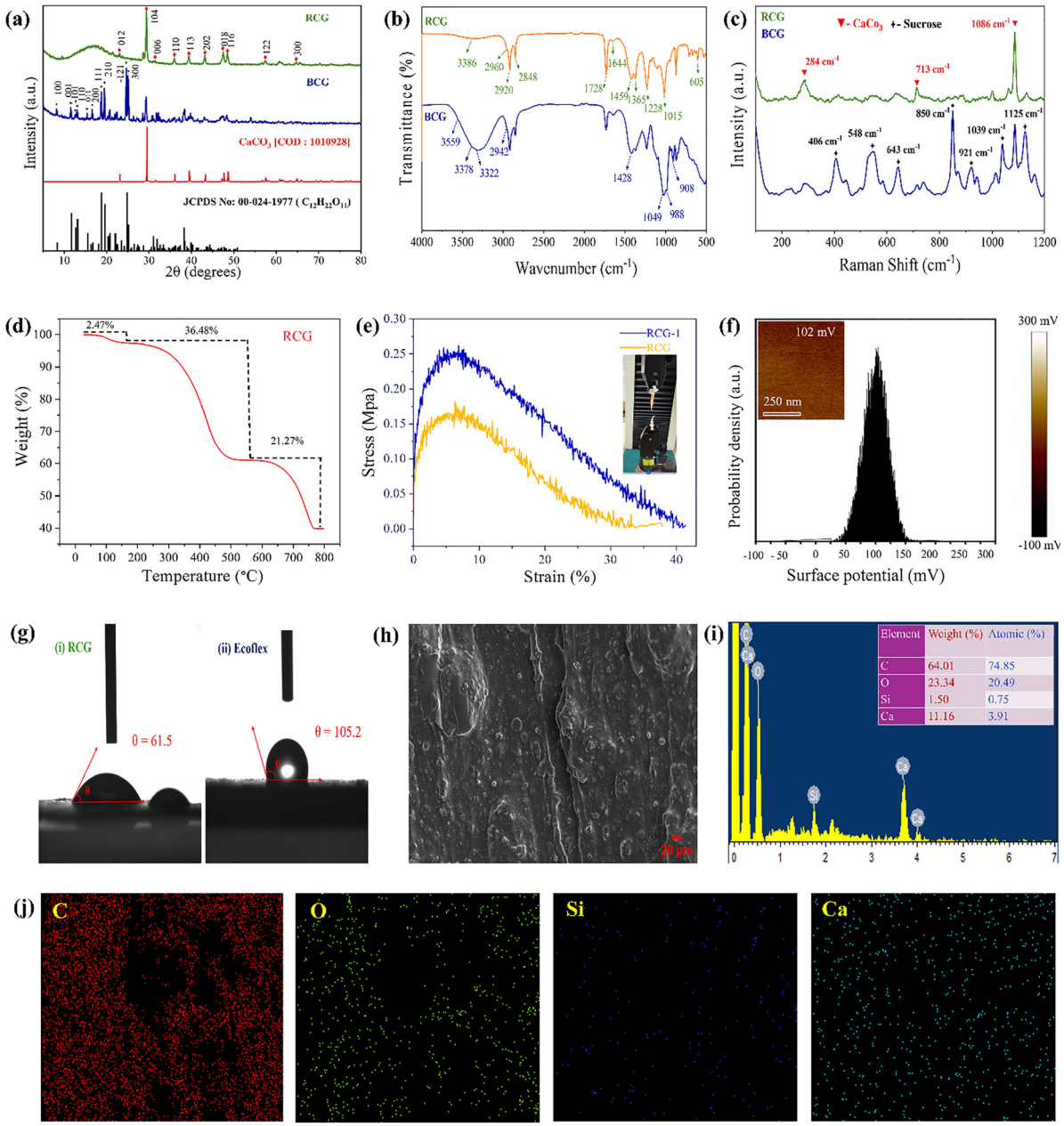

Fig. 2 A detailed chemical analysis of RCG: (a) X-ray diffraction analysis, (b) FTIR analysis, (c) Raman spectroscopy analysis, (d) thermogravimetric analysis, (e) tensile stress test performance and (f) Kelvin probe force microscope analysis. (g) Contact angle measurement of RCG and Ecoflex. (h) Surface morphology image. (i) EDX analysis. (j) RCG elemental mapping.

conducted. As illustrated in Fig. S2 of the SI, the gum exhibited minimal degradation, indicating its resistance to biodegradation. The investigation into the solubility of waste chewing gum across various solvents is depicted in Fig. S3 of the SI. The gum showed no solubility in ethanol, DMSO, methanol, water, or acetonitrile. Conversely, it was dispersed when placed in acetone and toluene, while only a slight dispersion occurred in isopropyl alcohol. The study explored how waste chewing gum adheres to different surfaces, with the findings illustrated in Fig. S4 of the SI. The adhesion tests revealed that the gum can stick to a variety of materials, such as metal, plastic, glass, ceramic, and even human skin.

Furthermore, the elemental composition and relative concentrations of RCG were determined by energy-dispersive X-ray spectroscopy (EDX) analysis: 64.01 weight% of carbon (C) (74.85 atomic%), 23.34 weight% of oxygen (O) (20.49 atomic%), and 11.16 weight% of calcium (Ca) (3.91 atomic%), 1.50 weight% of (Si) (0.75 atomic%), as shown in Fig. 2i. The detailed elemental mapping of the RCG for C, O, Si, and Ca is shown in Fig. 2j.

RCG-TENG device fabrication and mechanism

TENGs transform external low-frequency mechanical motions or vibrations into electrical energy using the principles of

 This journal is © The Royal Society of Chemistry 2026

electrostatic induction and contact electrification.[44–46] When two dielectric materials with varying electron affinities come into contact or are rubbed together, charges are transferred between them. The material that loses electrons becomes positively charged, while the one that gains electrons acquires a negative charge. This process, called contact electrification, depends on the surface properties of the materials, their nature, the friction between them, and the applied force. As these materials interact, electrostatic induction occurs, leading to the formation of opposite charges on attached electrodes. The electrode connected to the positive material pulls in negative charges, while the electrode linked to the negative material draws in positive charges. Consequently, an external circuit experiences current flow owing to the electric potential difference created between the electrodes. Because of the constant contact, separation, or rubbing of the triboelectric materials, a periodic output of voltage or current is obtained. A capacitor can be used to store charges for energy harvesting, and the electrical energy produced can be used for a variety of sensing purposes.[47,48]

A schematic of the 3 × 3 cm^2 spring-assisted RCG and Ecoflex triboelectric nanogenerator (RCG-TENG) is shown in Fig. 3a. The detailed information about the RCG-TENG device fabrication is mentioned in the SI, Fig. S5(a–e). The RCG-based contact separation of the triboelectric basic working principle and signal generation are shown in Fig. 3b. The RCG and Ecoflex were used as positive and negative triboelectric layers, respectively. Both sides of the aluminum sheets were considered electrodes and connected to a wire. Fig. 3(b) illustrates that the system utilizes a contact-separation TENG mechanism, a commonly reported approach for generating electrical energy.[49] In the tribo-electrification process, Ecoflex, with its high negative electron affinity, tends to gain electrons, whereas RCG, with a large positive affinity, loses electrons. Consequently, when the TENG device experiences contact and separation at various harmonic frequencies, electricity is produced through contact electrification and electrostatic induction.[50]

RCG-TENG performance

The open-circuit voltage (V_{OC}) and short-circuit current (I_{SC}) are the two main parameters used to evaluate the electrical performance of the RCG-TENG. The V_{OC}, I_{SC}, and circuit-transferred

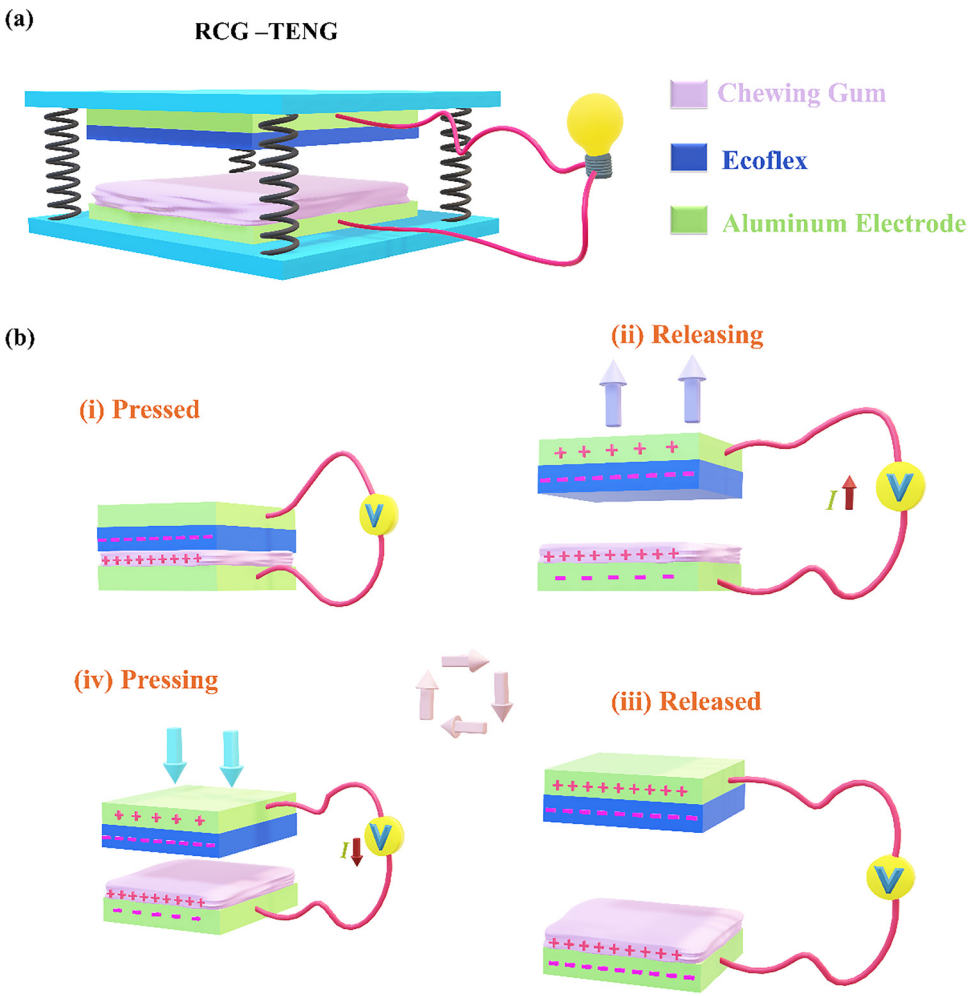

Fig. 3 Schematic of the chewing-gum-based triboelectric nanogenerator. (a) Spring-assisted RCG-TENG device structure. (b) Detailed working mechanism of the RCG-TENG.

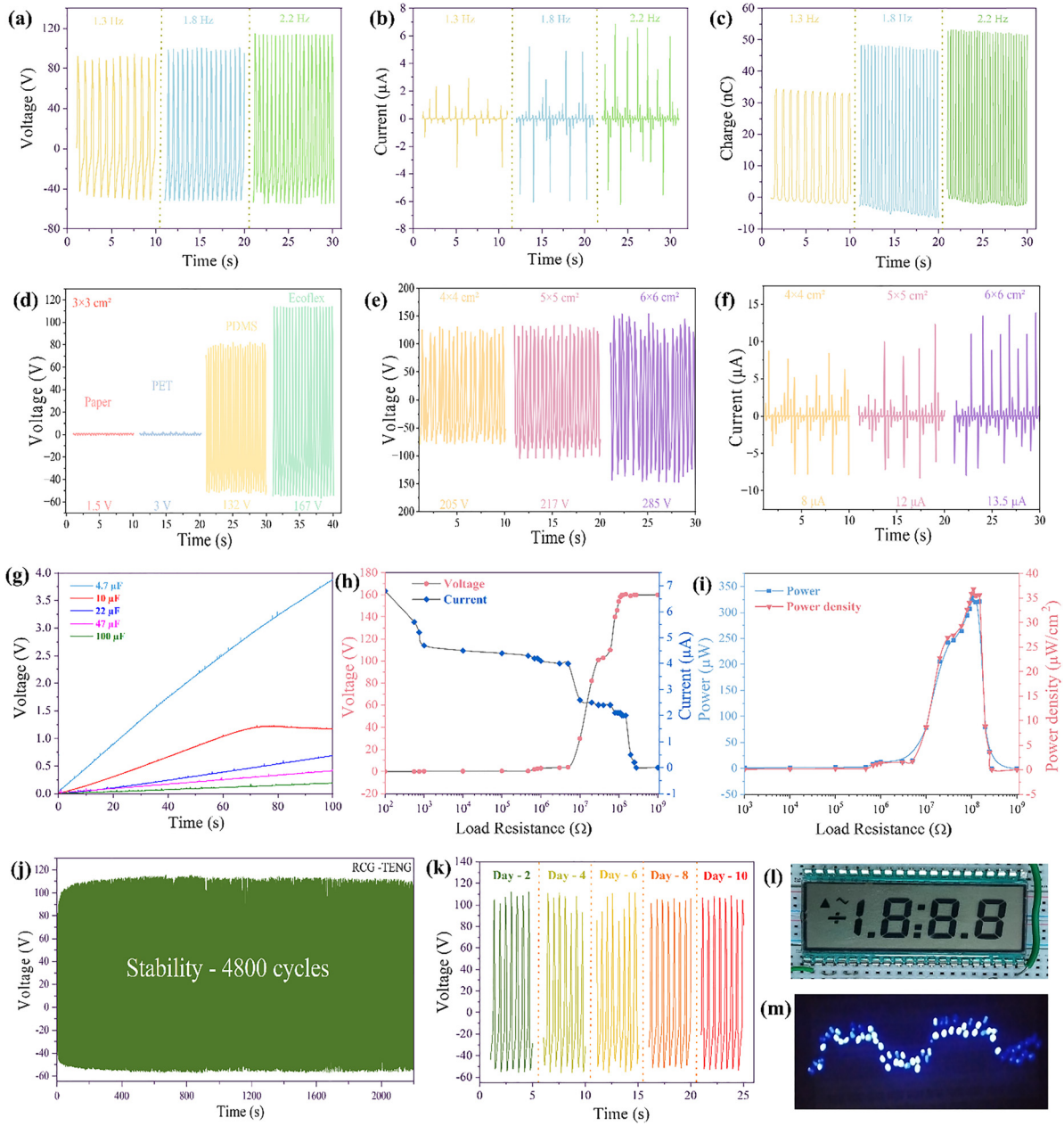

Fig. 4 The detailed triboelectric performance of the RCG. (a) Voltage, (b) current, (c) charge. (d) Voltage performance comparison of RCG against different triboelectric materials. (e) Area-dependent voltage performance of RCG-TENG. (f) Area-dependent current performance of RCG-TENG. (g) RCG-TENG capacitor charging analysis, (h) load analysis, (i) power and power density analysis. (j) Long-time cycle stability test. (k) Stability analysis for various days. (l) Powering an LCD. (m) Glowing LEDs *via* RCG-TENG.

charges were measured using a Keithley 6514 electrometer at various frequencies. Fig. 4a and b demonstrate that the peak-to-peak values for V_{OC} and I_{SC} reached 167 V and 6.9 μA, respectively, under continuous contact between the RCG and Ecoflex friction layer. The results for the RCG-TENG at different frequencies (1.3–2.2 Hz) are shown in Fig. 4a. The maximum voltage obtained corresponded to the RCG-TENG at a frequency of 2.2 Hz, and the peak-to-peak voltage was approximately 167 V. As the frequency increased, the peak-to-peak value of the open-circuit voltage also increased: 1.3 Hz (145 V), 1.8 Hz (152 V), and 2.2 Hz (167 V). The short-circuit current of the RCG TENG gradually increased with the frequency varying from 1.2 Hz (3 μA) to 1.8 Hz (5 μA) and 2.2 Hz (6.9 μA), as shown in Fig. 4b.

As shown in Fig. 4c, the charge nearly doubled when the frequency was increased from 1.3 Hz to 2.2 Hz (1.3 Hz, 34 nC; 1.8 Hz, 48 nC; 2.2 Hz, 52 nC). To determine the optimal triboelectric pair, RCG was evaluated against paper, PET, PDMS, and Ecoflex under the same conditions of an active area of 3 × 3 cm^2 and an operating frequency of 2.2 Hz. The output voltages recorded were 1.5, 3, 132, and 167 V for paper, PET, PDMS, and Ecoflex, respectively. The notably superior

 This journal is © The Royal Society of Chemistry 2026

performance of PDMS and Ecoflex is due to their more pronounced negative triboelectric properties, which enhance the triboelectric potential difference compared to RCG, as shown in Fig. 4d. To understand the large-scale effect of different active area sizes on the triboelectric performance, RCG-TENG devices were fabricated with dimensions of 4 cm × 4 cm, 5 cm × 5 cm, and 6 cm × 6 cm and subjected to tests at a consistent frequency of 2.2 Hz. As depicted in Fig. 4(e), the open-circuit voltage increased from 205 to 217 V, eventually reaching 285 V. Concurrently, Fig. 4(f) shows that the short-circuit current increased from 8 μA to 12 μA and then to 13.5 μA as the active area grew from 4 × 4 cm^2 to 5 × 5 cm^2 and 6 × 6 cm^2.

Fig. 4(g) illustrates how capacitors are charged over time using the RCG-TENG, with different capacitance values of 4.7 μF to 100 μF (4.7, 10, 22, 47, and 100 μF). Additionally, the electrical output of the RCG-TENG was evaluated by applying different load resistances. Commercial resistors ranging from 1 kΩ to 1 GΩ were connected in series with the device output to measure V_{OC} and I_{SC}. Furthermore, as shown in Fig. 4h, the V_{OC} clearly increases with increasing resistance; however, the I_{SC} shows an inverse trend, following Ohm's rule, $V = I \times R$. At a load resistance of approximately 100 MΩ, the instantaneous RCG-TENG demonstrated a maximum power of 346 μW and a power density of 35.55 μW cm^{-2}. This shows that the load resistance of the RCG-TENG and the 100 MΩ resistance match, which will be useful for real-time applications employing the device. The formula $P = VI$ was used to calculate the power output, where V is the voltage and I is the current across the load resistor. As shown in Fig. 4i, the power density (PD) of the RCG-TENG was calculated using the formula PD = P/A, where P represents the power of the RCG-TENG and A represents the area (3 × 3 cm^2). As depicted in Fig. 4j, the RCG-TENG device demonstrated exceptional voltage stability by consistently generating an output of 167 V for 4800 cycles. Every two days, the V_{OC} was consistently recorded between 160 and 167 V. This demonstrates the performance stability of the RCG-TENG. Therefore, the device can operate at any time with long durability and a stable electrical output, as shown in Fig. 4k. In the SI, Fig. S6, SEM illustrates the surface of the chewing gum layer both before and after extended TENG operation against Ecoflex, providing detailed insights into the surface analysis. The evaluation of the electrical resistance of recycled waste chewing gum was conducted using a two-probe measurement technique, with the findings detailed in Fig. S7 of the SI. Furthermore, it can power an LCD panel (40-pin TN-positive 5-digit segment) with a single tap (Fig. 4l). Video S1 shows an LCD powered by the RCG-TENG. The RCG-TENG could power more than 76 blue light-emitting diodes (Fig. 4m). Video S2 demonstrates the LED illumination achieved using the RCG-TENG.

Temperature and humidity performance

The humidity and temperature performances of the RCG TENG device were evaluated in a closed atmosphere to monitor various levels of temperature and humidity. In addition, we employed an ultrasonic mist maker humidifier with a Type-C port, a 5 V fogger atomization disc operating at 108 kHz, and a DIY mist atomizer USB mini board ultrasonic atomization module, all equipped with a PCB, to generate a humid atmosphere. To detect the humidity level in a closed atmosphere, we used a DHT 11 humidity sensor connected to the Arduino setup and a laptop, which allowed us to analyze humidity levels ranging from 50% to 98% relative humidity (RH). In addition, to obtain thermal images to confirm the humidity and thermal background environment, we utilized an FLIR E5 Pro, a commercial thermal imaging camera with Wi-Fi. The RCG-TENG device operates with a humidity performance that cycles between pressing and releasing at a frequency of 2.2 Hz, facilitated by a linear motor. At room temperature, the RCG-TENG provided a constant total voltage signal of approximately 167 V.

As the relative humidity (RH) gradually increased from 50% to 98%, the RCG-TENG device output gradually decreased because water molecules in the humid air impeded the flow of electrons between the chewing gum and Ecoflex layers, as shown in Fig. 5a(i). As humidity increased, the output voltage of the RCG-TENG consistently declined, with readings of about 167 V at 50% RH, 136 V at 60% RH, 112 V at 70% RH, 47.5 V at 80% RH, 30 V at 90% RH, and 7.5 V at 98% RH. The RCG-TENG output varied with changes in humidity, serving as an application for humidity sensing.[51,52] The RCG-TENG humidity setup image is shown in Fig. 5a(ii). A thermal image was captured to confirm that there was no interference from the heat observed in the humid atmosphere, as shown in Fig. 5a(iii).

To create a high-temperature environment at a controlled location, we utilized a hot-air gun (BST-898D dual LED) with a display screen. Furthermore, to detect the temperature in the closed atmosphere, we used a K-type thermocouple connected to a digital multimeter (HTC DM-97) to monitor the exact temperature. The RCG-TENG device operated effectively at temperatures of 40–80 °C. At room temperature, the RCG-TENG exhibited a stable output performance. However, from a temperature perspective, the RCG device exhibited a lower output performance because the heat environment reduced the output voltage. The RCG-TENG withstands temperatures up to 80 °C to provide less voltage performance; the RCG-TENG device provides voltage performance at higher temperatures and acts as a temperature sensor, as shown in Fig. 5b(i).[51,52] In addition, an image of the home-built setup of the temperature-controlled environment is shown in Fig. 5b(ii). The image of the thermal atmosphere with the RCG-TENG device provides strong proof that the RCG-TENG device will also perform well and withstand higher temperatures, as shown in Fig. 5b(iii).

RCG-TENG electroplating application

A self-sustaining electroplating system was developed by incorporating the RCG-TENG that was fabricated, as illustrated in Fig. 6a and b. In this research, electroplating was achieved through the simple mechanical energy generated by continuous tapping, without the need for external power. The generated electricity was connected to a DF06G rectifier, which converted the AC output to DC for electroplating applications. Subsequently, the electroplating cell received regulated power from the RCG-TENG, which helped deposit copper ions onto a

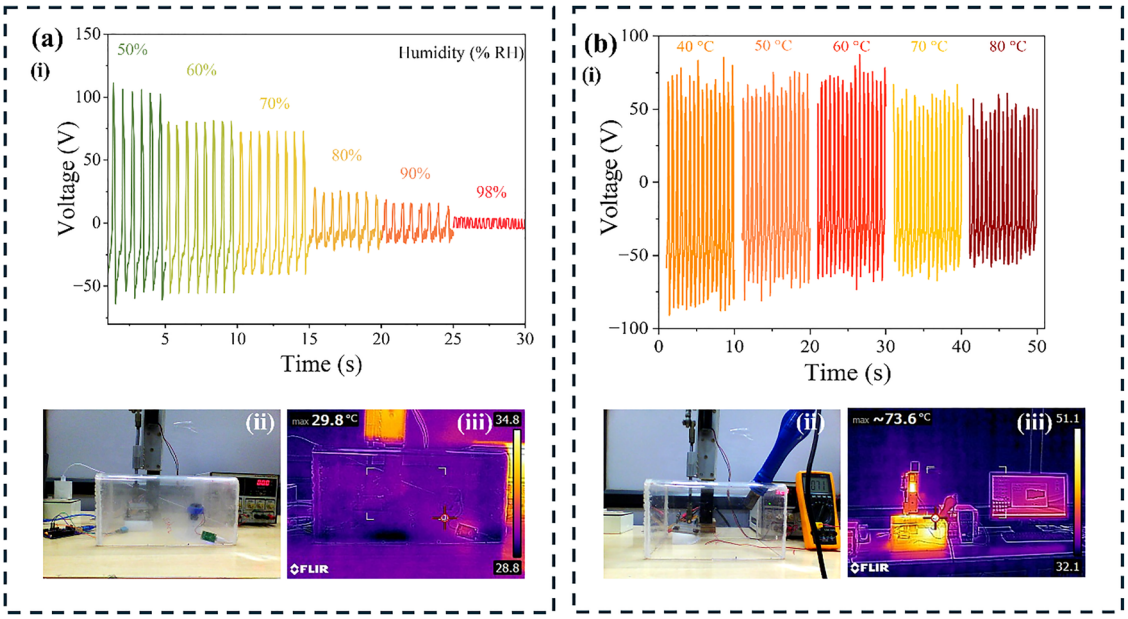

Fig. 5 The detailed humidity and thermal analysis of the RCG-TENG performance. (a) (i) RCG-TENG humidity analysis, (ii) humidity atmosphere setup, (iii) thermal camera image of the humidity environment. (b) (i) Temperature performance of the RCG-TENG, (ii) thermal atmosphere setup, (iii) thermal image of the temperature environment.

conductive aluminum substrate to create a consistent and uniform metal coating. The RCG-TENG converted mechanical energy into electrical energy, achieving 167 V and 6.9 μA of current. This energy can be utilized in a self-powered electroplating setup. This RCG-TENG system does not require an external power source, reduces costs, improves energy use, and supports recycling using renewable materials in the TENG. The RCG-TENG device is self-powered, highly versatile, and portable, making it suitable for application in areas with limited access to electricity. The industrialization of RCG-TENG has immense potential to transform electroplating procedures, making them more sustainable, environmentally friendly, and flexible enough to meet a range of commercial needs. This method promises highly reliable and high-quality copper coatings suitable for applications ranging from small to large scale in the electronics, spring, and industrial sectors.

To prepare the electrolyte solution, 0.5 mol of copper sulfate ($CuSO_4$) was added to 40 mL of H_2O and 3–5 drops of sulfuric acid (H_2SO_4) to supply Cu^{2+} ions.[53] There was a 3 cm space between the two electrodes, as shown in Fig. 6b(i). The pristine copper and aluminum electrodes had dimensions of 0.3 mm × 6 cm × 1.5 cm, as shown in Fig. 6b(ii).

The RCG-TENG device was linked to a rectifier, and an electroplating circuit was employed, utilizing a pure copper strip as the anode and an aluminum substrate as the cathode. Copper atoms are oxidized at the anode to generate Cu^{2+} ions, which then migrate through the electrolyte toward the aluminum cathode, with these ions subsequently being reduced at the cathode. The anode and cathode reactions are as follows:

$$\text{Cathode: } Cu(aq)^{2+} + 2^{e-}/Cu(s) \quad (1)$$

$$\text{Anode: } Cu(s)/Cu(aq)^{2+} + 2^{e-} \quad (2)$$

The electroplating process was studied for various durations without an external energy source. The RCG-TENG, operating at a frequency of 2.2 Hz *via* a linear motor, enabled continuous electroplating for 20 min, as shown in Fig. 6b(iii). Extending the process to 30 min (Fig. 6b(iv)) resulted in a more pronounced coating effect. Initially, 20 min of RCG-TENG electroplating on the aluminum substrate initiated copper deposition, and subsequent surface morphology analysis using SEM images at 10 and 20 μm, along with EDX, demonstrated the electroplating of copper onto the aluminum substrate, as shown in Fig. 6c(i) and (ii). After 20 min of operation, EDX analysis of the RCG-TENG verified the deposition of copper on the aluminum surface. The elemental weight percentages were 60.82% for aluminum and 26.10% for copper. Increasing the electroplating time to 30 min yielded a clear, visible, and uniform coating on the aluminum substrate. To clarify, we conducted SEM and EDX analyses of the copper-plated aluminum surface morphology shown in Fig. 6d(i) and (ii). Elemental analysis indicated the presence of 50.47 wt% aluminum and 36.27 wt% copper, thereby confirming the progressive electroplating of copper onto the aluminum substrate. The attached video (Video S3) provides real-time documentation of the RCG-TENG electroplating process.

The RCG-TENG serves as a sustainable power source in the proposed design, reducing the requirement for external electricity throughout the electroplating process by harnessing mechanical motion energy. To enhance the system's scalability and practicality, we verified that increasing the area leads to a corresponding increase in the output, confirming its potential for real-world applications. Furthermore, instead of relying on high-cost materials, we utilized RCG materials as triboelectric materials in the TENG device for electroplating applications,

 This journal is © The Royal Society of Chemistry 2026

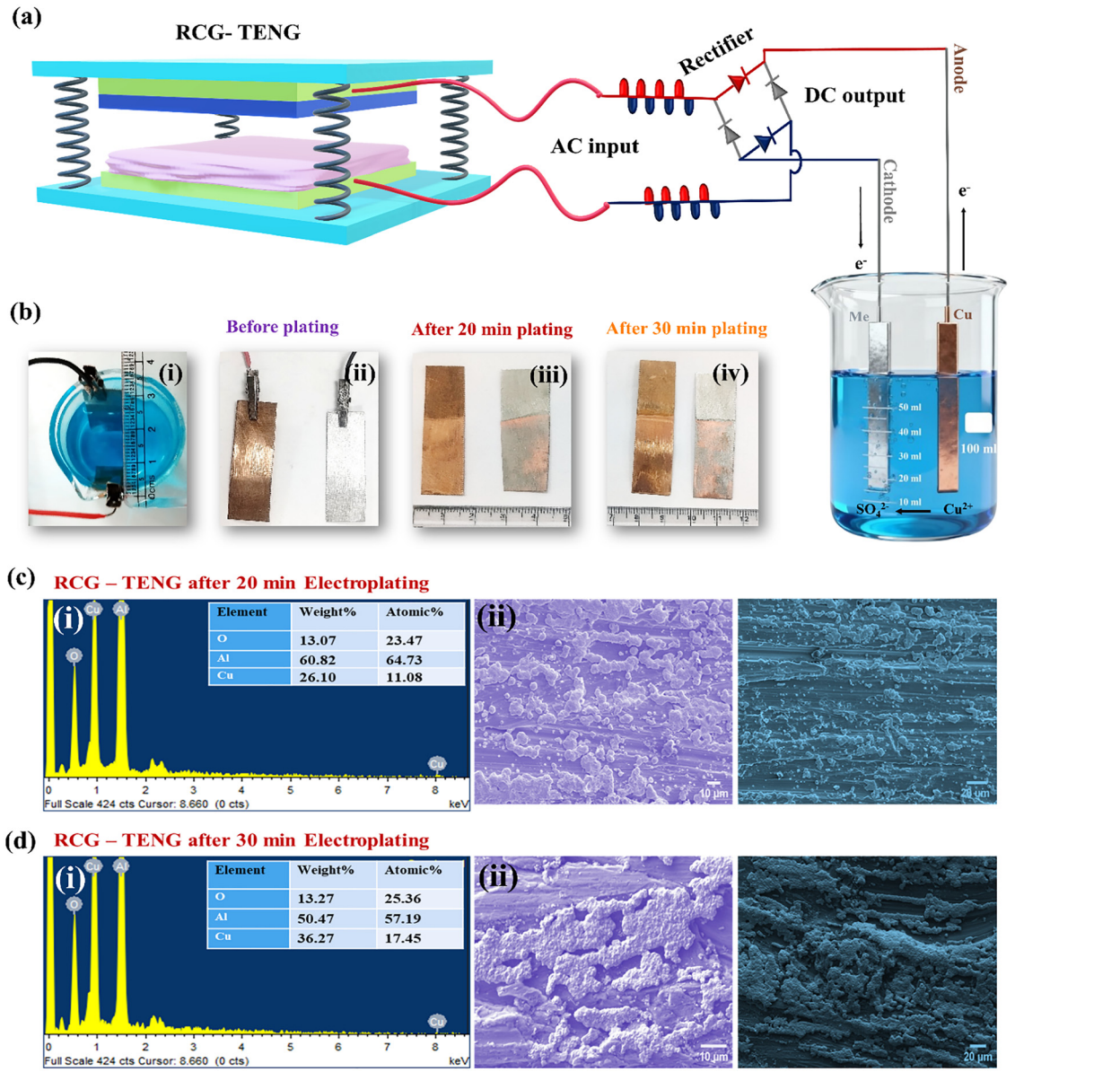

Fig. 6 (a) Schematic of the RCG-TENG electroplating application setup. (b) (i) Distance between the two electrodes, (ii) pristine aluminum and copper electrodes. (iii) After 20 min of electroplating *via* RCG-TENG and (iv) RCG-TENG after 30 min of electroplating. (c) SEM and EDX analysis after 20 min of electroplating. (d) SEM and EDX analysis after 30 min of electroplating.

showcasing a cost-effective and sustainable approach. Large-scale RCG-TENGs, for example, can supply the energy needed for metal deposition in electronic manufacturing, springs, and automobile parts in the electroplating industry, lowering dependency on external power sources and operating expenses. Another approach is to employ large-area, tile-based RCG-TENGs, which offer a creative means of harvesting energy from human walking to power the electroplating system. A comparison table of various bio-wastes,[54–57] food waste,[58–60] marine bio-waste,[61–64] household waste,[65–67] medical waste,[18,47,68] and textile waste is presented.[69–72] Also, various waste materials were converted into energy-harvesting devices *via* TENGs and various self-powered applications, as mentioned in SI S8. The TENG output performance of RCG was benchmarked against various commercially available triboelectric materials, and the results are presented in Table S1 of the SI. Among the various waste materials, the output voltage and current provided by the food waste RCG-TENG offer the highest output performance, as seen in the self-powered electroplating application.

Conclusion

Chewing gum is a non-biodegradable, water-insoluble, and non-digestible, as well as sticky material. Chewing gum waste that has been recycled is used to create practically useful products such as mugs and shoe soles. However, these products will again end up in the landfill, causing plastic pollution

and environmental damage. To prevent this, we have developed a tactile solution to use waste chewing gum as a tribo layer, enabling it to harvest energy through a TENG. Also, the RCG-TENG is utilized for temperature and humidity sensing, as well as for self-powered electroplating applications. Furthermore, RCG material has been explored through its chemical and mechanical characterization. We successfully determined the presence of the chewing gum filler material $CaCO_3$, as well as other complex compounds like binder, elastomer, and sweetening agent.

By harnessing the inherent properties of chewing gum, this innovative approach not only demonstrates a promising solution for mitigating environmental pollution but also contributes to the development of sustainable energy harvesting and storage solutions. The successful integration of RCG into TENGs underscores the possibility of transforming urban and rural waste into valuable, high-performance triboelectric materials, fostering a more resilient, circular, and sustainable economic system. Furthermore, this study highlights the potential for similar waste materials to be repurposed for energy applications, inspiring new avenues for waste management and sustainable development.

Experimental section

Materials

Discarded Boomer chewing gum waste (Wrigley, India) was collected and used as the triboelectric material for fabricating an RCG-based TENG. Absolute ethanol was obtained from AIC Specialties, Chennai, Tamil Nadu. Ecoflex (00-30) was purchased from Pearl Impex I-120, Sector – 2, DSIIDC, Bawana, Delhi. Deionized water and ethanol were used to purify the chewing gum waste.

Fabrication of recycled chewing gum into a positive triboelectric layer

The gum was usually chewed for 20 minutes, then the gum waste was recovered and cleaned with water and ethanol five times. RCG was subsequently dried in an oven at 45 °C. The RCG was applied to a 3×3 cm^2 aluminum substrate, which was connected to a copper wire to form the complete device structure, as shown in Fig. 1c.

Fabrication of Ecoflex 00-30 rubber compound into a negative triboelectric layer

A flexible, stretchable, strong, and soft Ecoflex film was prepared by mixing platinum-cure silicone polymer parts A and B, in a 1 : 1 ratio by weight, thoroughly stirring the mixture, and pouring it onto a flat mold.[22] The film was then cured at room temperature for 3 h and peeled off as the final thin Ecoflex film. A 1 mm thick, 3×3 cm^2 Ecoflex film was attached to an aluminum electrode connected to a copper wire.

Characterization and measurement

A Bruker D8 Advance, PANalytical X'Pert3 X-ray diffractometer (Germany) employing Ni-filtered Cu-Kα radiation in Bragg–Brentano geometry was used to assess the crystalline characteristics of the BCG and RCG samples. The chemical functional groups present on the surface and the interlayer bonding of RCG and BCG were examined by FTIR spectroscopy using a Shimadzu IRAffinity-1 instrument (Japan). The chemical compositions of RCG and BCG were analyzed by Raman spectroscopy using an Anton Paar Cora 5001 DUAL instrument. Thermogravimetric analysis was conducted on RCG using a TA Instruments SDT Q600 (USA) to assess their thermal stability and degradation characteristics. A single-column universal testing machine (H5KS, Tinius Olsen, UK) was utilized to assess the tensile strength and mechanical resilience of the RCG. An amplitude-modulated Bruker Kelvin probe force microscopy (AM-KPFM) system incorporating a thermal control stage was employed to perform surface potential mapping and work function measurements of the RCG, thereby assessing its charge distribution. A contact-angle goniometer (DMs-401, Kyowa Interface Science) was employed to determine the water contact angles of both the original Ecoflex and RCG samples. The surface morphology of the RCG was analysed through scanning electron microscopy (Carl Zeiss, EVO 18 Research, Germany). The fabricated RCG-TENG's electrical parameters were measured with a programmable electrometer (Keithley 6514, USA).

Author contributions

K. N. and A. C. conceived the idea, K. N. conducted material recycling, TENG device fabrication, and electrical characterization, wrote the first draft of the manuscript. Z. L. and P. G. validated and commented on the manuscript. K. N., A. C., Z. L., and P. G. contributed to reviewing and editing the manuscript. A. C., Z. L., and P. G. supervised the project.

Conflicts of interest

The authors state that they have no known financial conflicts of interest or personal relationships that could have affected the findings of this study.

Data availability

The data that support the findings of this study are available from the corresponding author upon reasonable request.

Supplementary information (SI): the materials, characterization results, and electrical performance data are available upon reasonable request from the authors. See DOI: https://doi.org/10.1039/d6tc01212d.

Acknowledgements

The Department of Science and Technology (DST), Science and Engineering Research Board (SERB), State University Research Excellence (SURE), Government of India (File number: SUR/2022/004324), along with the VIT International Research Fund Scheme (VIN) Award for FY2024-2025, provided support for this research to facilitate international collaboration opportunities.

 This journal is © The Royal Society of Chemistry 2026

We appreciate the research facilities and technical assistance provided by VIT University, Vellore. In addition, the author is grateful to the 'Nanosensors and Nanoenergy Lab' (NSNE Lab) group members Nimmi Sharma, Sushmitha Benny, Nishath Bagum, and Sayyed Abdul Basith. The authors also acknowledge Pearl Research Park (PRP) Bio Medical Instrumentation Lab (BMI Lab). In this study, the graphical abstract parts of images and most of the scientific illustrations were crafted using Blender (Version 5.1.2; Blender Foundation, Amsterdam, The Netherlands). The authors extend their sincere thanks to the Blender Foundation for creating and distributing this open-source software free of charge. Schematic diagrams in Fig. 1(c) and Fig. 6(a), including the electroplating glass beaker, were generated using ChatGPT Go, followed by arrangement in Microsoft PowerPoint and review by the authors for scientific accuracy.

References

1 A. S. Roy, *Curr. World Environ.*, 2021, **16**, 916–927.
2 L. Satari, A. Guillén, À. Vidal-Verdú and M. Porcar, *Sci. Rep.*, 2020, **10**, 16846, DOI: 10.1038/s41598-020-73913-4.
3 N. Konar, I. Palabiyik, O. S. Toker and O. Sagdic, Elsevier Ltd, 2016, **55**, 29–38. , DOI: 10.1016/j.tifs.2016.07.003.
4 R. W. Hartel, J. H. Von Elbe and R. Hofberger, *Confectionery Science and Technology*, Springer, Cham, 2018.
5 N. Kashyap and M. R. Thomas, *J. Case Res.*, 2017, **8**(1), 23–27.
6 Functional Chewing Gums Market Size & Outlook, 2027, https://www.grandviewresearch.com/horizon/outlook/functional-chewing-gums-market-size/global.
7 The Problem | Lemelson, https://lemelson.mit.edu/teams/blog/problem.
8 Z. Li, A. Yu, J. Zhai and Z. L. Wang, *Adv. Mater.*, 2025, **37**, 2412671, DOI: 10.1002/adma.202412671.
9 H. Wang, S. Li, Y. Zhang, M. Zhang, H. Wang, X. Liang, H. Lu and Y. Zhang, *SmartSys*, 2025, **1**, e3, DOI: 10.1002/sys3.3.
10 J. Zhu, M. Zhu, Q. Shi, F. Wen, L. Liu, B. Dong, A. Haroun, Y. Yang, P. Vachon, X. Guo, T. He and C. Lee, *EcoMat*, 2020, **2**, e12058, DOI: 10.1002/eom2.12058.
11 G. Zhu, J. Chen, Q. Jing and Z. L. Wang, *Nano Energy*, 2015, **14**, 126–138, DOI: 10.1016/j.nanoen.2014.11.050.
12 A. A. Khan, A. Mahmud and D. Ban, *IEEE Trans. Nanotechnol.*, 2019, **18**, 21–36.
13 S. R. Begum and A. Chandrasekhar, *iScience*, 2024, **27**, 108878, DOI: 10.1016/j.isci.2024.108878.
14 Z. Li, A. Yu, Q. Zhang and J. Zhai, *Int. J. Extrem. Manuf.*, 2024, **6**, 052003, DOI: 10.1088/2631-7990/ad4f32.
15 P. K. Nitha and A. Chandrasekhar, *ACS Appl. Electron. Mater.*, 2024, **6**, 5314–5327.
16 P. Munirathinam and A. Chandrasekhar, *Micromachines*, 2023, **14**, 592, DOI: 10.3390/mi14030592.
17 R. F. Sagade Muktar Ahmed, S. B. Mohan, S. Madanahalli Ankanathappa, M. Shivanna, P. Viswanathan, H. C. S. Manjunatha, Y. S. Vidya, A. Chandrasekhar and K. Sannathammegowda, *ACS Appl. Electron. Mater.*, 2023, **5**, 5885–5897.
18 A. Chandrasekhar, A. Basith, V. Vivekananthan, G. Khandelwal, N. Prashant, M. J. Raj, Y. Purusothaman and S. J. Kim, *Nano Energy*, 2024, **123**, 109379, DOI: 10.1016/j.nanoen.2024.109379.
19 Z. Ding, M. Zou, P. Yao, Z. Zhu and L. Fan, *Micromachines*, 2021, **12**, 1314, DOI: 10.3390/mi12111314.
20 M. U. Bukhari, K. Riaz, K. Q. Maqbool, R. Ahmed, A. Khan, B. Wang and A. Bermak, *ACS Appl. Bio Mater.*, 2024, **7**, 5939–5947.
21 Y. Han, Y. Han, X. Zhang, L. Li, C. Zhang, J. Liu, G. Lu, H. D. Yu and W. Huang, *ACS Appl. Mater. Interfaces*, 2020, **12**, 16442–16450.
22 S. A. Basith and A. Chandrasekhar, *Adv. Mater. Technol.*, 2023, **8**, 2300495, DOI: 10.1002/admt.202300495.
23 M. Navaneeth, S. Potu, A. Babu, R. K. Rajaboina, K. Uday Kumar, H. Divi, P. Kodali and K. Balaji, *Environ. Science: Adv.*, 2023, **2**, 848–860.
24 L. Zhang, Y. Yu, G. P. Eyer, G. Suo, L. A. Kozik, M. Fairbanks, X. Wang and T. L. Andrew, *Adv. Mater. Technol.*, 2016, **1**, 1600147, DOI: 10.1002/admt.201600147.
25 M. Singh, S. Kumar, A. Kafle, K. Garg, P. Sharma, C. C. Reddy and T. C. Nagaiah, *J. Mater. Chem. A*, 2025, **13**, 6549–6559.
26 B. Cheng and P. Wu, *ACS Appl. Mater. Interfaces*, 2021, **13**, 6731–6738.
27 M. A. Darabi, A. Khosrozadeh, Q. Wang and M. Xing, *ACS Appl. Mater. Interfaces*, 2015, **7**, 26195–26205.
28 J. Zhao, J. Li, Q. Zeng, H. Wang, J. Yu, K. Ren, Z. Dai, H. Zhang, J. Zheng and R. Hu, *Macromol. Rapid Commun.*, 2022, **43**, 2200234, DOI: 10.1002/marc.202200234.
29 J. Zhu, L. Li, M. Dong, Z. Zeng and L. Sun, *Colloids Surf., A*, 2023, **675**, 132128, DOI: 10.1016/j.colsurfa.2023.132128.
30 N. Nciri, N. Kim and N. Cho, *Polymers*, 2021, **13**, 1963, DOI: 10.3390/polym13121963.
31 M. Bragaglia, L. Paleari, J. A. Berrocal, F. R. Lamastra and F. Nanni, *J. Appl. Polym. Sci.*, 2023, **140**, e53750, DOI: 10.1002/app.53750.
32 Gumdrop Ltd – Give gum a second life, https://gumdropltd.com/.
33 Used Chewing Gum Receptacle, https://shop.terracycle.com/en-US/products/gum-receptacle.
34 R. P. D'Amelia, J. J. Stroz and R. Kachikian, *US Pat.*, 4452820A, 1984.
35 C. Shen, J. H. Song, B. Padovani and D. W. Record, *US Pat.*, 20090017160A1, 2009.
36 S. Wei, V. Pintus and M. Schreiner, *J. Anal. Appl. Pyrolysis*, 2012, **97**, 158–163.
37 M. Feng, X. Hu, Y. Yin, Y. Liang, J. Niu and J. Yao, *Polymers*, 2022, **14**, 2842, DOI: 10.3390/polym14142842.
38 N. Nciri, N. Kim and N. Cho, *Polymers*, 2021, **13**, 1963, DOI: 10.3390/polym13121963.
39 S. Sukirno, S. Pebriani, D. Febriantini, A. S. Nugraha and B. Purnomo, *Rasayan J. Chem.*, 2021, **14**, 40–46, DOI: 10.31788/RJC.2021.1456550.

40 D. R. Phillips and L. D. Morgret, *Eur. Pat.*, EP 3316698 B1, 2023.

41 B. Guven, S. Durakli-Velioglu and İ. H. Boyaci, *Gıda*, 2019, **44**, 274–290.

42 A. Pal, H. Kim, S. Suresh, P.-H. Wei, A. M. Al-Kabbany, D. Choi and Z.-H. Lin, *J. Am. Chem. Soc.*, 2026, **148**, 3063–3076.

43 R. Janardhana, F. Akram, Z. Guler, A. Adaval and N. Jackson, *Materials*, 2025, **18**, 3037, DOI: 10.3390/ma18133037.

44 W. Wang, X. Feng, K. Wang and L. Li, in Proceedings – 2019 4th International Conference on Control, Robotics and Cybernetics, CRC 2019, Institute of Electrical and Electronics Engineers Inc., 2019, pp. 157–161.

45 Z. Lin, W. Long, L. J. Chen, S. Niu and Y. Zi, Green Energy and Technology, *Triboelectric Nanogenerators*, Springer International Publishing, 2016, DOI: 10.1007/978-3-319-40039-6.

46 Z. L. Wang, *Handbook of Triboelectric Nanogenerators*, Springer International Publishing, 2023, pp. 1–30.

47 S. A. Basith and A. Chandrasekhar, *Nano Energy*, 2023, **108**, 108183, DOI: 10.1016/j.nanoen.2023.108183.

48 A. Chandrasekhar, N. R. Alluri, M. S. P. Sudhakaran, Y. S. Mok and S. J. Kim, *Nanoscale*, 2017, **9**, 9818–9824.

49 V. Vivekananthan, A. Chandrasekhar, N. R. Alluri, Y. Purusothaman and S. J. Kim, *Nanoscale Adv.*, 2020, **2**, 746–754.

50 Z. Saadatnia, E. Esmailzadeh and H. E. Naguib, *Adv. Eng. Mater.*, 2019, **21**, 1700957, DOI: 10.1002/adem.201700957.

51 Y. Su, G. Xie, S. Wang, H. Tai, Q. Zhang and H. Du, in *2017 IEEE SENSORS*, pp. 1–3, DOI: 10.1109/ICSENS.2017.8234280.

52 J. Si, J. Yang, Y. Chen, N. Hu, Y. Yang, Y. Wu, Q. A. Huang and L. Han, *J. Mater. Chem. C*, 2024, **12**, 11640–11647.

53 N. Madathil, A. Babu, M. Velupula, A. Kulandaivel, R. K. Rajaboina, U. K. Khanapuram, K. C. Devarayapalli and D. S. Lee, *Sustain. Energy Fuels*, 2025, **9**, 4364–4374.

54 S. Jakmuangpak, T. Prada, W. Mongkolthanaruk, V. Harnchana and S. Pinitsoontorn, *ACS Appl. Electron. Mater.*, 2020, **2**, 2498–2506.

55 Z. Ding, M. Zou, P. Yao, Z. Zhu and L. Fan, *Micromachines*, 2021, **12**, 1314, DOI: 10.3390/mi12111314.

56 N. R. Alluri, N. P. M. Joseph Raj, G. Khandelwal, V. Vivekananthan and S.-J. Kim, *Nano Energy*, 2020, **73**, 104767, DOI: 10.1016/j.nanoen.2020.104767.

57 Y. Chen, Y. Jie, J. Wang, J. Ma, X. Jia, W. Dou and X. Cao, *Nano Energy*, 2018, **50**, 441–447.

58 W. J. Kim, S. W. Kim, S. H. Park, Y. H. Doh and Y. J. Yang, *J. Korean Soc. Manuf. Process Eng.*, 2022, **21**, 9–15.

59 P. Jaiban, S. Khumtrong, P. Kongchana, T. Theethuan, S. Lokakaew, P. Phutthami, A. Watcharapasorn, R. Guo and A. S. Bhalla, *Mater. Lett.*, 2022, **325**, 132862, DOI: 10.1016/j.matlet.2022.132862.

60 J. Jiao, Q. Lu, Z. Wang, Y. Qin and X. Cao, *Nano Energy*, 2021, **79**, 105411, DOI: 10.1016/j.nanoen.2020.105411.

61 J. N. Kim, J. Lee, T. W. Go, A. Rajabi-Abhari, M. Mahato, J. Y. Park, H. Lee and I. K. Oh, *Nano Energy*, 2020, **75**, 104904, DOI: 10.1016/j.nanoen.2020.104904.

62 Y. Han, Y. Han, X. Zhang, L. Li, C. Zhang, J. Liu, G. Lu, H. D. Yu and W. Huang, *ACS Appl. Mater. Interfaces*, 2020, **12**, 16442–16450.

63 Y. Pang, F. Xi, J. Luo, G. Liu, T. Guo and C. Zhang, *RSC Adv.*, 2018, **8**, 6719–6726.

64 G. Khandelwal, T. Minocha, S. K. Yadav, A. Chandrasekhar, N. P. M. Joseph Raj, S. C. Gupta and S.-J. Kim, *Nano Energy*, 2019, **65**, 104016, DOI: 10.1016/j.nanoen.2019.104016.

65 P. Zhang, W. Zhang and H. Zhang, *Sens. Actuators, A*, 2021, **322**, 112633, DOI: 10.1016/j.sna.2021.112633.

66 X. Feng, Q. Li and K. Wang, *ACS Appl. Mater. Interfaces*, 2021, **13**, 400–410.

67 G. Khandelwal, A. Chandrasekhar, N. R. Alluri, V. Vivekananthan, N. P. Maria Joseph Raj and S. J. Kim, *Appl. Energy*, 2018, **219**, 338–349.

68 J. Swain, S. Hajra, N. Das, P. Parhi, S. Panda, A. Priyadarshini, J. Panda, A. K. Sahu, P. Alagarsamy, V. Vivekananthan, H. J. Kim and R. Sahu, *Energy Technol.*, 2023, **11**, 2300498, DOI: 10.1002/ente.202300498.

69 G. M. Rani, C.-M. Wu, K. G. Motora and R. Umapathi, *J. Cleaner Prod.*, 2022, **363**, 132532, DOI: 10.1016/j.jclepro.2022.132532.

70 M. Sahu, S. Hajra, S. Panda, M. Rajaitha, B. K. Panigrahi, H.-G. Rubahn, Y. K. Mishra and H. J. Kim, *Nano Energy*, 2022, **97**, 107208, DOI: 10.1016/j.nanoen.2022.107208.

71 W. Paosangthong, M. Wagih, R. Torah and S. Beeby, *Nano Energy*, 2019, **66**, 104148, DOI: 10.1016/j.nanoen.2019.104148.

72 T. Zhou, C. Zhang, C. B. Han, F. R. Fan, W. Tang and Z. L. Wang, *ACS Appl. Mater. Interfaces*, 2014, **6**, 14695–14701.

 This journal is © The Royal Society of Chemistry 2026